



Published in final edited form as:

J Biomol NMR. 2019 April ; 73(3-4): 141–153. doi:10.1007/s10858-019-00237-5.

Hybridization of TEDOR and NCX MAS solid-state NMR experiments for simultaneous acquisition of heteronuclear correlation spectra and distance measurements

T. Gopinath¹, Songlin Wang¹, John Lee¹, Hideki Aihara¹, and Gianluigi Veglia^{1,2,*}

¹Department of Biochemistry, Molecular Biology, and Biophysics, University of Minnesota, Minneapolis, MN 55455.

²Department of Chemistry, University of Minnesota, Minneapolis, MN 55455.

Abstract

Magic angle spinning (MAS) solid-state NMR (ssNMR) spectroscopy is a major technique for the characterization of the structural dynamics of biopolymers at atomic resolution. However, the intrinsic low sensitivity of this technique poses significant limitations to its routine application in structural biology. Here we achieve substantial savings in experimental time using a new subclass of Polarization Optimized Experiments (POEs) that concatenate TEDOR and SPECIFIC-CP transfers into a single pulse sequence. Specifically, we designed new 2D and 3D experiments (2D TEDOR-NCX, 3D TEDOR-NCOCX, and 3D TEDOR-NCACX) to obtain distance measurements and heteronuclear chemical shift correlations for resonance assignments using only one experiment. We successfully tested these experiments on N-Acetyl-Val-Leu dipeptide, microcrystalline U-¹³C,¹⁵N ubiquitin, and single- and multi-span membrane proteins reconstituted in lipid membranes. These pulse sequences can be implemented on any ssNMR spectrometer equipped with standard solid-state hardware using only one receiver. Since these new POEs speed up data acquisition considerably, we anticipate their broad application to fibrillar, microcrystalline, and membrane-bound proteins.

Keywords

Solid-state NMR; Magic Angle Spinning; Polarization Optimized Experiments; TEDOR; SPECIFIC-CP; NCA; NCO; DARR; Microcrystalline Proteins; Membrane Proteins; Sarcolipin; *Succinate-Acetate permease Protein*

INTRODUCTION

Magic angle spinning (MAS) solid-state NMR (ssNMR) spectroscopy plays a central role in the characterization of structures, motions, and interactions of biological macromolecules such as fibrillar, microcrystalline, and membrane proteins^{1–6}. Sensitivity and resolution, however, still limit its routine application to membrane proteins, where motion and sample

*To whom correspondence should be addressed: Gianluigi Veglia, Department of Biochemistry, Molecular Biology & Biophysics, University of Minnesota, 6-155 Jackson Hall, MN 55455., Telephone: (612) 625-0758., Fax: (612) 625-2163., vegli001@umn.edu.

heterogeneity complicate the interpretation of NMR spectra. In addition to this, the high lipid-to-protein ratios essential to maintain the functional integrity of membrane proteins also dilute the protein content of MAS samples and substantially increase the experimental time necessary to obtain high-quality spectra. As a result, NMR of membrane proteins requires longer acquisition times compared to fibrils or microcrystalline protein preparations.

To overcome these challenges and reduce experimental time, we developed Polarization Optimized Experiments (POEs), a class of pulse sequences that make the best out of nuclear polarization⁷⁻¹⁰. POEs are ideal for MAS experiments on U-¹³C,¹⁵N labeled biomolecules at low-to-moderate spinning rates, which are often crucial to preserve enzymatic function³. POEs enable the acquisition of multiple 2D and 3D NMR spectra simultaneously in a single experiment, resulting in a substantial saving of experimental time. A key element of POEs is the simultaneous cross-polarization (SIM-CP) scheme that matches Hartmann-Hahn conditions for ¹H, ¹³C, and ¹⁵N contemporarily to generate an additional ¹⁵N polarization (N_z) that remains stored along the z-axis for several milliseconds due to its relatively long longitudinal relaxation time (T_1)⁷. Therefore, after the main experiment is recorded (first acquisition), the N_z polarization is utilized to generate one or more nD spectra within the same pulse program^{8,10}. Analogously, ¹³C polarization generated by SIM-CP can be stored along the z-axis (C_z) and utilized for multiple experiments as previously demonstrated^{7,11}. The FIDs originating from POEs are usually saved in different memory allocations and processed into separate spectra^{7,9}. The straightforward implementation on commercial NMR spectrometers equipped with only one receiver and probes for bio-solids (Low-E or E-free) made POEs appealing to the broader NMR community¹²⁻¹⁴. In fact, other groups extended POE to ¹H detected experiments to obtain a considerable gain in sensitivity and time efficiency¹⁵⁻¹⁷.

Our original POEs were designed to record a ¹³C-¹³C homonuclear correlation spectrum as the main experiment, followed by single or multiple ¹³C-¹⁵N correlation spectra in subsequent acquisitions. Here, we expanded the POE toolkit¹⁸ by hybridizing transferred echo double resonance (TEDOR)¹⁹⁻²² and spectrally induced filtering in combination with cross-polarization (SPECIFIC-CP)²³ transfer elements to record ¹³C-¹⁵N correlation experiments in the first and subsequent multiple acquisitions. With these hybridized pulse sequences, we were able to combine distance measurements and heteronuclear chemical shift correlation experiments. We successfully performed these experiments on U-¹³C,¹⁵N microcrystalline ubiquitin as well as two U-¹³C,¹⁵N labeled membrane proteins: sarcolipin (SLN), a single-pass transmembrane protein²⁴, and succinate-acetate permease (SatP), with six transmembrane helices²⁵⁻²⁷.

MATERIALS AND METHODS

The expression, purification, and microcrystalline preparation of recombinant U-¹³C,¹⁵N ubiquitin were carried out as reported by Igumenova *et al.*²⁸. Recombinant SLN was expressed in *E. coli* bacteria using minimal M9 media enriched with ¹³C glucose (Sigma) and ¹⁵N ammonium chloride (Sigma) as reported previously²⁹. Succinate-acetate permease (SatP) was expressed and purified from *E. coli* bacteria as a SUMO fusion protein. Briefly,

E. coli SatP was cloned into a pE-SUMOpro-Amp (LifeSensors) vector and expressed in *E. coli* BL21(DE3) cells. Cells were grown to an optical density (OD) at 600 nm of 1.0 at 37 °C in M9 media with 50 mg/L ampicillin then induced with 1 mM isopropyl-D-thiogalactoside (IPTG). All purifications were carried out on ice. Cells from 2 L of culture were harvested and lysed by sonication in 50 mM Tris buffer (pH 7.4), 500 mM NaCl, and 0.5 mM phenylmethylsulfonyl fluoride (PMSF). SatP was solubilized from whole lysed cells in 50 mM Tris buffer (pH 7.4), 500 mM NaCl, 10% glycerol; and 200 mM Octyl Glucoside (OG, Anatrace) or 10 mM Octyl Glucose Neopentyl Glycol (OGNG, Anatrace) for 2 h at 4 °C. After centrifugation at 60,000 x g, solubilized SatP protein in the supernatant was batch-bound to Ni-NTA resin (Qiagen) for 1 h, washed with 25 bed volumes of 50 mM Tris buffer (pH 7.4), 300 mM NaCl, 10% glycerol, 40 mM OG, and 40 mM imidazole, then eluted with 250 mM Tris buffer (pH 7.4), 300 mM NaCl, 10% glycerol, 40 mM OG; and 300 mM imidazole. Imidazole was removed using a BioRad Econo-Pac 10DG desalting column and the histidine-tagged SUMO was removed by digestion with histidine-tagged SUMO protease for 12 h at 4 °C. The protein sample was batch bound to Ni-NTA resin and the flow through containing SatP was concentrated and further purified on a GE Superdex 200 gel filtration column with a mobile phase of 50 mM Tris buffer (pH 7.4), 100 mM NaCl, 10% glycerol, and 40 mM OG.

For NMR experiments, approximately 0.6 mg of SLN or 8 mg SatP were reconstituted into 12 mg of 1,2-dimyristoyl-sn-glycero-3-phosphocholine (DMPC, Avanti Polar Lipids) at lipid-to-protein ratios of 100 and 40, respectively³. All the experiments were implemented on Agilent and Bruker spectrometers operating at a ¹H Larmor frequency of 600 MHz. Experiments on U-¹³C, ¹⁵N SLN, U-¹³C, ¹⁵N ubiquitin, and U-¹³C, ¹⁵N NAVL dipeptide were acquired using a 3.2 mm scroll coil MAS probe with 25 µL sample volume. Spectra of U-¹³C, ¹⁵N SatP were acquired using a 1.3 mm Bruker MAS probe with 4 µL sample volume. All data were acquired with a recycle delay of 3 s and MAS rate (ν_r) set to 12.5 kHz, which corresponds to an 80 µs rotor period (τ_r). The maximum RF amplitude on the ¹H channel was set to 100 kHz, which corresponds to a 90° pulse of 2.5 µs; whereas the RF amplitude for the ¹³C and ¹⁵N channels was set to 41.6 kHz and corresponds to a 90° pulse of 6 µs. During the REDOR period^{30,31}, 180° pulses of 12 µs were applied on both ¹³C and ¹⁵N channels. The 180° pulses on the ¹⁵N channel were phase cycled using the XY-4 scheme³². CP and SIM-CP contact times were set to 500 µs, during which the RF amplitudes of ¹³C and ¹⁵N were set to 35 kHz, and the ¹H RF amplitude was ramped from 90 to 100%, with the center of the ramp set to 60 kHz. During TEDOR mixing, t_1 evolution, and t_2 acquisition periods, a SPINAL-64 ¹H decoupling sequence was used on the ¹H channel with 100 kHz RF amplitude³³. The t_2 acquisition times for ¹³C detection were set to 15 ms with 10 µs dwell time; whereas the ¹⁵N signal was evolved during t_1 with 320 µs (equal to $4 \times \tau_r$) dwell time for 32 increments, corresponding to a maximum t_1 evolution time of 10.24 ms. For the U-¹³C, ¹⁵N NAVL sample, 16 increments of t_1 were acquired with a dwell time of 640 µs. The SPECIFIC-CP transfer between ¹⁵N and ¹³C α or ¹³CO was achieved using a tangent-shaped ramp pulse on ¹³C and a constant amplitude pulse applied on ¹⁵N, with CW (continuous wave) decoupling applied on ¹H nuclei using 100 kHz RF amplitude. The offset for ¹³C was set to 50 and 175 ppm for NCA and NCO transfer periods, respectively. The RF amplitudes of ¹³C were set to 18.75 kHz ($1.5 \times \nu_r$) and 43.75 kHz ($3.5 \times \nu_r$) for NCA and

NCO transfers, respectively, whereas the ^{15}N RF amplitude was arrayed around 31.25 kHz ($2.5 \times \nu_r$) to obtain the maximum intensity of signals³⁴. All elements in the TEDOR sequence were synchronized with the rotor frequency $\nu_r = 1/\tau_r$. For 1D and 2D TEDOR experiments, the t_{mix} was set to 1.28 ms ($16 \times \tau_r$), which gave the maximum $^{13}\text{C}\alpha$ signal. The ^{15}N dwell time (t_1) was set to $4 \times \tau_r$ (320 μs) during which a ^1H decoupling with 100 kHz RF amplitude was applied. The two periods (z-filters) were set to 240 μs ($3 \times \tau_r$) with ^1H RF set to 12.5 kHz to facilitate rapid dephasing of ^{13}C transverse magnetization¹⁹. Before and after t_1 evolution, a pair of 90° pulses with a total length of 24 μs were applied. To avoid desynchronization, an additional τ delay after t_1 evolution was set to 216 μs ($3 \times \tau_r - 24 \mu\text{s}$)^{19,21}. The pseudo-3D TEDOR-NCACX-NCOCX experiment was performed on U- ^{13}C , ^{15}N crystalline NAVL using 16 t_1 increments and a dwell time of 640 μs . The parameters for the 3D TEDOR experiments were similar to the 2D TEDOR with the t_{mix} period arrayed from 1.28 to 17.92 ms¹⁹. The 2D spectra of U- ^{13}C , ^{15}N SLN, U- ^{13}C , ^{15}N SatP, and U- ^{13}C , ^{15}N ubiquitin were acquired with 512, 400, and 128 scans, respectively. The pseudo-3D TEDOR-NCACX-NCOCX experiment on U- ^{13}C , ^{15}N NAVL was acquired using 64 scans. A ^1H RF amplitude of 12.5 kHz (ν_r)³⁵ was used for ^{13}C , ^{13}C -DARR mixing periods.

RESULTS

Simultaneous acquisition of TEDOR and NCX experiments.

The original pulse sequence for the z-filtered (ZF) TEDOR experiment uses ^1H - ^{13}C CP as a preparation period (Figure 1A)¹⁹. In contrast, the new hybrid pulse sequence, TEDOR-NCX (Figure 1B), starts with the SIM-CP sequence that creates both ^{13}C and ^{15}N polarization from the ^1H spin bath, which are utilized to record TEDOR and NCA (or NCO) experiments in the 1st and 2nd acquisition, respectively. The coherence transfer pathways for the hybrid TEDOR-NCX experiment can be described using the product operator formalism as follows:

$$\begin{aligned}
& \sum_z H \xrightarrow{(90^\circ_{\phi_1=y})^H - \text{SIM-CP}} C_x + N_x \xrightarrow{(90^\circ_{-y})^N} C_x + N_z \\
& \xrightarrow{\text{REDOR}(t_{\text{mix}}/2)} C_x \cdot \cos(\omega t_{\text{mix}}/2) + 2C_y N_z \cdot \sin(\omega t_{\text{mix}}/2) + N_z \\
& \xrightarrow{(90^\circ_x)^C - \Delta - (90^\circ_{\phi^*=y})^N} 2C_y N_x \cdot \sin(\omega t_{\text{mix}}/2) + N_x \\
& \xrightarrow{t_1 - (90^\circ_{\phi_2=-y})^C - \tau - (90^\circ_x)^N} \left[-2C_y N_z \cdot \sin(\omega t_{\text{mix}}/2) + N_z \right] e^{i\omega_N t_1} \\
& \xrightarrow{\text{REDOR}(t_{\text{mix}}/2)} \left[-2C_y N_z \cdot \sin(\omega t_{\text{mix}}/2) \cdot \cos(\omega t_{\text{mix}}/2) + C_x \cdot \sin^2(\omega t_{\text{mix}}/2) + N_z \right] e^{i\omega_N t_1} \\
& \xrightarrow{(90^\circ_{-y})^C - \Delta - (90^\circ_y)^C - t_2} \left[C_x \cdot \sin^2(\omega t_{\text{mix}}/2) \cdot e^{i\omega_N t_1} \cdot e^{i\omega_C t_2} \right]_{\text{1st Acquisition}}^{\text{TEDOR}} + N_z \cdot e^{i\omega_N t_1} \\
& \xrightarrow{(90^\circ_y)^N - [\text{SPECIFIC CP}]^{\text{NCA/NCO}}} C_x \\
& \cdot e^{i\omega_N t_1} \xrightarrow{t_2} \left[C_x \cdot e^{i\omega_N t_1} \cdot e^{i\omega_C t_2} \right]_{\text{2nd Acquisition}}^{\text{NCA/NCO}}
\end{aligned}$$

(1)

The ^{13}C and ^{15}N chemical shifts are represented by ω_C and ω_N , whereas ω represents the effective ^{13}C - ^{15}N dipolar coupling. After SIM-CP, the ^{15}N polarization is stored along the z-axis (N_z) by applying a 90° pulse, whereas the ^{13}C transverse polarization is evolved through REDOR mixing ($t_{\text{mix}}/2$) to create an antiphase ^{13}C single quantum coherence ($2C_y N_z$). Note that the ^{15}N polarization remains along the z-axis after the 180° pulses are applied on the ^{15}N channel during the REDOR mixing period. The coherence transfer from ^{13}C to ^{15}N ($2C_z N_x$) is obtained by a pair of 90° pulses applied on both ^{13}C and ^{15}N channels, with the latter flipping N_z into the transverse spin operator N_x . Both in-phase and antiphase ^{15}N single-quantum operators (N_x and $2C_z N_x$) evolved simultaneously according to their chemical shifts during t_1 and under ^1H decoupling. The States quadrature detection in the t_1 dimension is achieved by switching the phase ϕ^* of the ^{15}N pulse between y and -x prior to t_1 evolution. After t_1 evolution, a pair of 90° pulses is applied on ^{13}C and ^{15}N , which converts the antiphase operator $2C_z N_x$ into $2C_y N_z$ and the N_x operator into N_z . A τ period is used to compensate for rotor desynchronization caused by the duration of the 90° pulses. An identical REDOR mixing period ($t_{\text{mix}}/2$) converts the antiphase spin operator $2C_y N_z$ into the in-phase C_x operator, which gives rise to the TEDOR signal detected during the 1st t_2 acquisition period. Note that in equation 1, the spin coherences such as $[C_x \cdot \cos(\omega \cdot t_{\text{mix}}/2)]$, $[2C_y N_z \cdot \sin(\omega \cdot t_{\text{mix}}/2) \cdot \cos(\omega \cdot t_{\text{mix}}/2)]$, and other multiple quantum terms (not shown) created

by homonuclear ^{13}C - ^{13}C J -couplings are eliminated by ^{15}N phase cycling (ϕ_2) and periods as shown in Figures 1A and 1B¹⁹. The TEDOR mixing period t_{mix} (equation 1, and Figure 1) can be adjusted to optimize the ^{15}N - ^{13}C transfer. For example, one bond ^{15}N - ^{13}C transfer requires up to 1.2 ms mixing period. After this first acquisition, a τ_1 -90°- τ_1 sequence ($\tau_1 = 3$ ms) is applied on the ^{13}C channel to remove any residual ^{13}C magnetization⁷. The N_z is then tilted into the transverse plane by a 90° pulse followed by a SPECIFIC-CP transfer from ^{15}N to ^{13}Ca or ^{15}N to ^{13}CO , which is detected in the second acquisition period (t_2).

Figures 1C and 1D show 1D TEDOR and NCA spectra of U- ^{13}C , ^{15}N SLN obtained from TEDOR and the hybrid TEDOR-NCA pulse sequences. These spectra were obtained by setting the t_1 evolution period to zero and using a mixing time (t_{mix}) of 1.28 ms. The integrated intensities were normalized to the corresponding intensities of the TEDOR spectrum to determine possible signal losses. For the ^{13}Ca region (50–70 ppm), we obtained integrated signal intensities of 1.00 and 0.99 using conventional TEDOR and TEDOR-NCA sequences, respectively, whereas the corresponding values for the ^{13}CO region (165–180 ppm) were 1.00 and 0.94. The marginal loss of ^{13}CO signal intensity detected for the TEDOR-NCA pulse sequence is due to the SIM-CP transfer implemented in the preparation period, which usually reduces the intensity of the ^{13}CO signals by 5–10%^{7,10}. Figure 1D also shows the 1D NCA spectrum from the 2nd acquisition of the TEDOR-NCA experiment. In this case, the normalized integrated intensities of ^{13}Ca region from TEDOR (1st acquisition) and NCA (2nd acquisition) were 1.00 and 0.95, respectively. Note that these two spectra can be added to increase the S/N ratio by 38%.

To understand the effects of temperature on ^{13}C signal intensities, we acquired a series of 1D TEDOR and NCA spectra of U- ^{13}C , ^{15}N SLN and U- ^{13}C , ^{15}N SatP at temperatures above and below the phase transition of the DMPC lipid bilayer (Figure 2). For U- ^{13}C , ^{15}N SatP, the integrated intensities of 1D NCA spectra (red) are about 10–30% higher than the corresponding TEDOR spectra (blue). In contrast, the intensities of the TEDOR and NCA spectra performed on U- ^{13}C , ^{15}N SLN are virtually identical. The highest peak intensities and resolution for both proteins were obtained at 2°C, where DMPC is in the gel phase. The signal intensities for both samples gradually decrease upon reaching DMPC's liquid crystalline phase (i.e., 20–30°C), with signal intensities of both TEDOR and NCA spectra following similar trends.

A comparison of the 2D TEDOR-NCA experiments on U- ^{13}C , ^{15}N SLN and U- ^{13}C , ^{15}N SatP are reported in Figures 3 and 4. Specifically, Figure 3A and 3B show 2D TEDOR-NCA spectra of U- ^{13}C , ^{15}N SLN. After summing the TEDOR and NCA data sets, we obtained an average net increase in signal intensity of 32% (Figure 3C). Note that the sum of the two spectra also increases the noise level by $\sqrt{2}$, therefore intensities were scaled down by a factor of 0.707 ($1/\sqrt{2}$) when quantifying signal in the spectrum of Figure 3C. The peak positions of U- ^{13}C , ^{15}N SLN match our previous resonance assignments obtained with the 3D-DUMAS-NCACX-CANCO experiment^{10,36}. The total time for acquiring 2D TEDOR-NCA spectra was 27.8 hours and the additional 2nd acquisition increased the experimental time by only 16 minutes. In contrast, to record only a single spectrum with the conventional 2D TEDOR experiment would have taken 27.5 hours. We repeated the 2D TEDOR-NCA experiment for U- ^{13}C , ^{15}N SatP (Figure 4A). SatP is a significantly larger membrane protein,

with six transmembrane domains arranged in ordered hexamers in the lipid membrane. The relative intensity of the 2D NCA for the ^{13}C (40–70 ppm) and ^{15}N (100–140 ppm) spectral regions is ~30% higher than the TEDOR spectrum. The sum of TEDOR and NCA spectra obtained has a signal intensity gain of 60% with respect to the TEDOR spectrum alone (Figure 4A). This intensity gain is apparent in Figure 4C, where 1D cross sections taken at 119 ppm of the ^{15}N dimension are reported for TEDOR and TEDOR+NCA spectra.

Simultaneous acquisition of TEDOR, NCA, and NCO correlation experiments.

The hybridization of TEDOR and SPECIFIC-CP enables the concatenation of TEDOR, NCA, and NCO experiments for their simultaneous detection (Figure 5A). The pulse sequence is an extension of 2D TEDOR-NCA and utilizes the residual ^{15}N polarization stored on the z-axis by a 90° pulse after NCA transfer. The first and second acquisitions enable the recording of TEDOR and NCA spectra, respectively. After the second acquisition, the residual ^{15}N polarization ('orphan' or 'afterglow' polarization)^{8,37} is transferred to ^{13}CO by a 90° pulse and the NCO transfer using SPECIFIC-CP, which creates an NCO correlation experiment recorded in the third acquisition period. As shown previously, 30–35% of signal intensity is retained by the residual ^{15}N polarization after the NCA transfer^{8,37}, hence the third spectrum is typically 30–35 % less intense than the second spectrum. To demonstrate the performance of the hybridized TEDOR-NCA-NCO pulse sequence, we used a U- ^{13}C , ^{15}N microcrystalline ubiquitin sample (Figure 5B). The integrated intensities of 2D NCA and NCO spectra (red and green, respectively) are 1.2 and 0.7 times, respectively, that of the TEDOR spectrum (blue). As shown in Figures 4 and 5 for both U- ^{13}C , ^{15}N SatP and U- ^{13}C , ^{15}N ubiquitin, TEDOR-NCA, TEDOR-NCO or TEDOR-NCA-NCO experiments offer an efficient way to assign Pro resonances. In fact, Pro resonances, which are typically located between 128 to 135 ppm in the ^{15}N dimension, display substantially higher signals in the TEDOR spectra compared to NCA spectra. This is due to inefficient ^{15}N CP caused by the absence of directly bound protons to the imino groups of Pro residues. In contrast, TEDOR detects Pro residues more efficiently by using ^{13}C CP followed by a CANCA or CONCO pathway.

Simultaneous acquisition of 3D-TEDOR, NCACX, and NCOCX experiments.

Using a similar strategy, we hybridized 3D TEDOR, NCACX, and NCOCX experiments (Figure 6). In this pulse sequence, a 3D TEDOR spectrum is acquired during the first acquisition, whereas NCACX and NCOCX are recorded in the second acquisition. Typically, 3D TEDOR requires 12 to 18 mixing periods, which can be synchronized with NCACX and NCOCX experiments having different DARR mixing times. Figure 6B, shows a table with fourteen mixing times for the 3D TEDOR experiment in the first acquisition. For the second acquisition, the 3D TEDOR experiment is synchronized with seven NCACX and seven NCOCX experiments, with DARR mixing times set to 0, 10, 50, 100, 150, 200, and 300 ms. As a benchmark, we used U- ^{13}C , ^{15}N N-acetyl-Valine-Leucine (NAVL) dipeptide with an unlabeled acetyl group. Figure 7A and 7B show the strip plots extracted from the 3D-TEDOR, NCACX and NCOCX spectra of NAVL. The corresponding intensities of the TEDOR cross peaks observed between Val N to Val C β , and Leu N to Val C β as a function of the mixing time are reported in Figure 8A. Even at short mixing times, the signal-to-noise ratio for the cross-peaks is greater than 15 and the resulting experimental error bars are

contained within the symbols. The peak intensities were fit to simulated curves using the equations reported in reference ¹⁹, where the intra-residue distance between Val N to Val C β was set to 2.7 Å, and the inter-residue distance between Leu N to Val C β was set to 3.5 Å. These distances are in close agreement with those reported in the literature ¹⁹. Note that the NAVL crystal used in this work contains 100% U-¹³C, ¹⁵N labeled molecules, which may cause slight deviations from the theoretical TEDOR curves due to inter-molecular dipolar couplings. Figure 8B shows the plot of the intensities of ¹³C-¹³C cross-peaks between Val C α to Val C β and Val C α to Leu C α obtained from the NCACX spectra at various DARR mixing times (Figure 7B). The peak intensities were normalized with the Val C α peak of the NCA spectrum (Figure 7B). As expected, the Val C α -C β cross peak has the highest intensity at shorter DARR mixing time (50 ms). On the other hand, the inter-residue cross peak between Val C α to Leu C α requires 150 ms DARR mixing time to build up completely and reaches a plateau due to spin diffusion. Note that in general the DARR peak intensities are less quantitative than TEDOR experiments; therefore, it is advisable to acquire multiple DARR spectra at different mixing times and classify peak intensities as short-, medium-, and long-range distances of up to 10 Å ^{38,39}. Note that in the 3D experiment, the initial polarization of NCACX and NCOCX experiments can be slightly different due to the effect of 180° pulses on ¹⁵N z-magnetization during the TEDOR mixing. Figure 9 shows the intensity variation of 1D NCA spectra of NAVL sample acquired in the second acquisition at different TEDOR mixing times. Even at longer mixing times (10–15 ms), the loss of intensity is less than 10% with respect to the initial mixing period of 1.28 ms.

DISCUSSION

In ssNMR, the efficiency of CP transfer periods is often compromised by ¹H-¹H spin diffusion. As a result, only a portion of nuclear polarization generated in the preparation periods is converted into observable coherences. Pines and Waugh were the first to exploit the residual polarization of the rich ¹H spin bath to acquire multiple ¹H-enhanced CP spectra and increase the signal-to-noise ratio of solid samples ⁴⁰. More recently, Tang and Nevzorov proposed a comparable scheme to enhance the sensitivity of oriented membrane protein samples ⁴¹. In spite of that, most pulse sequences are inefficient and many spin operators remain essentially undetectable (orphan spin operators) ^{18,42,43}.

During the past decade, our group has developed POEs to recover orphan spin operators for signal enhancements or acquire multiple spectra from single pulse sequences in both oriented and MAS ssNMR ^{7,10,188,11,42,43}. POE experiments in MAS are based on the SIM-CP preparation period, where the rich ¹H spin bath enables the simultaneous generation of ¹³C and ¹⁵N polarization pathways, which are then utilized for acquiring 2D multidimensional experiments using DUMAS pulse sequences ^{7,10,18}. In addition, POE utilizes ¹³C and ¹⁵N residual polarization pathways resulting from N-C CP periods and generates four to eight multi-dimensional spectra (MEIOSIS and MAESTOSO-8) ^{8,11}. Other groups have paralleled our efforts. For instance, the use of ¹⁵N residual polarization pathways have also been utilized by Ramachandran and co-workers for acquiring multiple experiments under fast MAS conditions ¹⁵. Similarly, the ‘afterglow’ pulse sequences developed by the Traaseth lab exploits the residual ¹⁵N polarization and simultaneously records NCA and NCO spectra ³⁷. The afterglow phenomenon has been used in concert with

SIM-CP for the MEOSIS scheme to record four 2D spectra simultaneously [DARR, NCACX, NCO and CA(N)CO] ⁸.

Our previously published POEs were able to generate a ¹³C-¹³C homonuclear correlated spectrum in the first acquisition and exploit the additional ¹⁵N or ¹³C polarization for single or multiple ¹³C-¹³C and ¹³C-¹⁵N correlation experiments ^{7,10,11,44}. By hybridizing TEDOR and NCX experiments in this work, we introduced a novel way to obtain multiple ¹⁵N-¹³C experiments for both resonance assignments and distance measurements. This new sub-class of POEs takes advantage of the small dipolar couplings (~ 1 kHz) associated with NCA or NCO spin pairs that enable the ¹⁵N-¹³C polarization transfer. In the original TEDOR pulse sequence, the ¹⁵N-¹³C dipolar recoupling is achieved by using a pair of REDOR mixing periods ^{19,30}; whereas the NCX (NCA or NCO) transfer uses a selective ¹⁵N-¹³C recoupling via Hartmann-Hahn matching using SPECIFIC-CP ^{23,45}. A key difference between TEDOR and NCX experiments is the initial preparation period. While TEDOR uses the ¹³C polarization originating from ¹H-¹³C CP, the NCX experiment uses the ¹⁵N polarization from ¹H-¹⁵N CP. The hybridized 2D and 3D TEDOR-NCX pulse sequences combine these two pathways for generating multiple ¹⁵N-¹³C correlation spectra.

The optimal performance of TEDOR and SPECIFIC-CP depends on the sample characteristics as well as quality of the NMR hardware (RF homogeneity and probes). For instance, longer transfer periods for SPECIFIC-CP (3–6 ms) may cause inefficient polarization transfer due to fast $T_{1\rho}$ relaxation and/or RF inhomogeneity ^{46,47}. In the most favorable cases, the latter problem can be overcome by using shaped pulses to suppress RF inhomogeneity during the NC transfer ^{46,48,49}. Note also that TEDOR transfer relies on the efficiency of 180° pulses and T_2 relaxation of the antiphase spin operators, which is relatively short for biomolecular solids. A detailed description of how RF inhomogeneity and sample characteristics affect the ssNMR experiments can be found in the references ^{50–52}. In our hands, however, we found that NCA transfer is more efficient than TEDOR for membrane proteins such as SatP (Figures 2 and 4). Therefore, the performance of these two techniques may depend mostly on sample heterogeneity and protein dynamics. In fact, the RF inhomogeneity compensated shaped pulses can also be applied to hybrid TEDOR-NCX pulse sequences. From a technical viewpoint, the application of POEs with multiple acquisitions may result in an increase of RF duty cycles; however, the pulse sequences designed here are within the power limits indicated for the commercially available E-free or low-E MAS ssNMR probes ^{12–14}.

In recent years, several different techniques have been proposed to speed up the acquisition of MAS ssNMR experiments. Among those, the conjoined ultra-fast MAS with proton detection ^{53–58} and sparse protein perdeuteration ⁵⁹ have produced spectra with the resolution and sensitivity comparable to those of liquid-state NMR. Additionally, Ishii and co-workers introduced the use of paramagnetic relaxation agents, reducing recycle delays and increasing the repetition times ⁶⁰. However, the most significant sensitivity enhancement for biomolecular solids has been achieved using dynamic nuclear polarization (DNP) ⁶¹, with recent applications on several biological macromolecules. The pulse sequences presented here can be implemented with the above techniques in a synergistic way to boost

even more the sensitivity and resolution of multidimensional NMR experiments for biomolecular samples.

CONCLUSIONS

In conclusion, we introduced a new sub-class of POE pulse sequences for simultaneous acquisition of multiple NC correlation spectra using a single receiver. Both 2D and 3D TEDOR experiments are combined with NC or NCC sequences for recording ^{15}N - ^{13}C fingerprints as well as simultaneous measurements of ^{15}N - ^{13}C and ^{13}C - ^{13}C distances. These experiments are not alternatives to the existing approaches for sensitivity enhancement; rather they provide novel strategies that can be combined with the current methods to speed up data acquisition and lead to faster structure determination of proteins in different folded states.

ACKNOWLEDGEMENTS

This work was supported by the National Institute of Health (GM 64742 to G.V. and R35 GM118047 to H.A.). Many thanks to Dr. D. Weber for critical reading and editing the manuscript.

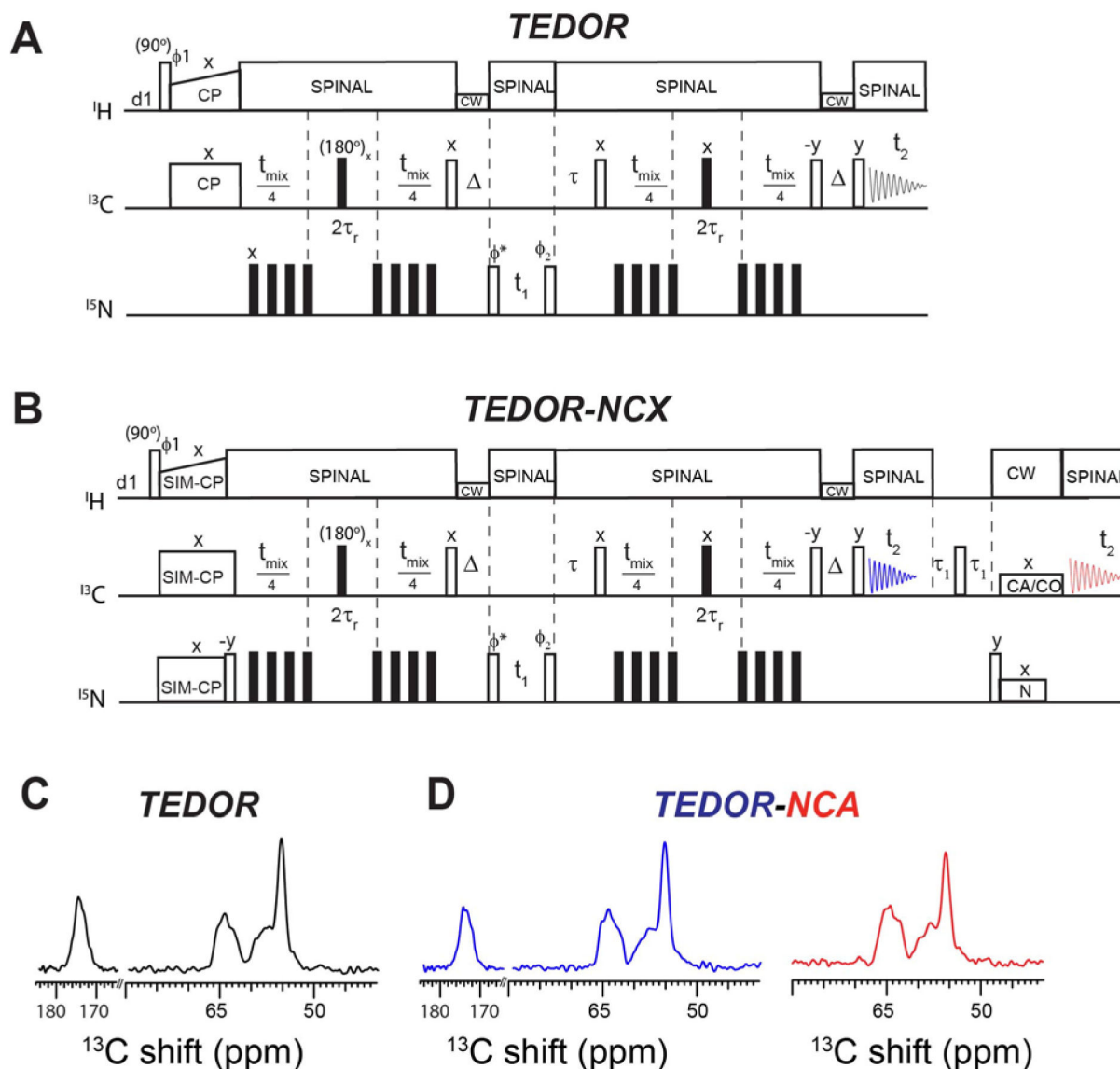
REFERENCES

1. Ader C et al. Structural rearrangements of membrane proteins probed by water-edited solid-state NMR spectroscopy. *J Am Chem Soc* 131, 170–6 (2009). [PubMed: 19063626]
2. Castellani F et al. Structure of a protein determined by solid-state magic-angle-spinning NMR spectroscopy. *Nature* 420, 98–102 (2002). [PubMed: 12422222]
3. Gustavsson M et al. Allosteric regulation of SERCA by phosphorylation-mediated conformational shift of phospholamban. *Proc Natl Acad Sci U S A* 110, 17338–43 (2013). [PubMed: 24101520]
4. Hong M, Zhang Y & Hu F Membrane protein structure and dynamics from NMR spectroscopy. *Annu Rev Phys Chem* 63, 1–24 (2012). [PubMed: 22136620]
5. Hu F, Luo W & Hong M Mechanisms of proton conduction and gating in influenza M2 proton channels from solid-state NMR. *Science* 330, 505–8 (2010). [PubMed: 20966251]
6. Wang S & Ladizhansky V Recent advances in magic angle spinning solid state NMR of membrane proteins. *Prog Nucl Magn Reson Spectrosc* 82C, 1–26 (2014).
7. Gopinath T & Veglia G Dual acquisition magic-angle spinning solid-state NMR-spectroscopy: simultaneous acquisition of multidimensional spectra of biomacromolecules. *Angew Chem Int Ed Engl* 51, 2731–5 (2012). [PubMed: 22311700]
8. Gopinath T & Veglia G Orphan spin operators enable the acquisition of multiple 2D and 3D magic angle spinning solid-state NMR spectra. *J Chem Phys* 138, 184201 (2013). [PubMed: 23676036]
9. Gopinath T & Veglia G Experimental Aspects of Polarization Optimized Experiments (POE) for Magic Angle Spinning Solid-State NMR of Microcrystalline and Membrane-Bound Proteins. *Methods Mol Biol* 1688, 37–53 (2018). [PubMed: 29151203]
10. Gopinath T & Veglia G 3D DUMAS: simultaneous acquisition of three-dimensional magic angle spinning solid-state NMR experiments of proteins. *J Magn Reson* 220, 79–84 (2012). [PubMed: 22698806]
11. Gopinath T & Veglia G Multiple acquisitions via sequential transfer of orphan spin polarization (MAeSTOSO): How far can we push residual spin polarization in solid-state NMR? *J Magn Reson* 267, 1–8 (2016). [PubMed: 27039168]
12. Gor'kov PL et al. Using low-E resonators to reduce RF heating in biological samples for static solid-state NMR up to 900 MHz. *J Magn Reson* 185, 77–93 (2007). [PubMed: 17174130]
13. McNeill SA, Gor'kov PL, Shetty K, Brey WW & Long JR A low-E magic angle spinning probe for biological solid state NMR at 750 MHz. *J Magn Reson* 197, 135–44 (2009). [PubMed: 19138870]

14. Stringer JA et al. Reduction of RF-induced sample heating with a scroll coil resonator structure for solid-state NMR probes. *J Magn Reson* 173, 40–8 (2005). [PubMed: 15705511]
15. Bellstedt P et al. Solid state NMR of proteins at high MAS frequencies: symmetry-based mixing and simultaneous acquisition of chemical shift correlation spectra. *J Biomol NMR* 54, 325–35 (2012). [PubMed: 23180049]
16. Das BB & Opella SJ Simultaneous cross polarization to (^{13}C) and (^{15}N) with (^1H) detection at 60kHz MAS solid-state NMR. *J Magn Reson* 262, 20–26 (2016). [PubMed: 26705905]
17. Sharma K, Madhu PK & Mote KR A suite of pulse sequences based on multiple sequential acquisitions at one and two radiofrequency channels for solid-state magic-angle spinning NMR studies of proteins. *J Biomol NMR* 65, 127–141 (2016). [PubMed: 27364976]
18. Gopinath T & Veglia G Orphan Spin Polarization: A Catalyst for High-Throughput Solid-State NMR Spectroscopy of Proteins. *Annual Reports on NMR Spectroscopy* 89, 103–21 (2016).
19. Jaroniec CP, Filip C & Griffin RG 3D TEDOR NMR experiments for the simultaneous measurement of multiple carbon-nitrogen distances in uniformly $(^{13}\text{C},^{15}\text{N})$ -labeled solids. *J Am Chem Soc* 124, 10728–42 (2002). [PubMed: 12207528]
20. Rienstra CM et al. De novo determination of peptide structure with solid-state magic-angle spinning NMR spectroscopy. *Proc Natl Acad Sci U S A* 99, 10260–5 (2002). [PubMed: 12149447]
21. Hong M & Griffin RG Resonance assignments for solid peptides by dipolar-mediated C-13/N-15 correlation solid-state NMR. *Journal of the American Chemical Society* 120, 7113–7114 (1998).
22. Andrew W Hing S, and Schaefer Jacob. Transferred-echo double-resonance NMR. *Journal of Magnetic Resonance* 96, 205–209 (1992).
23. Baldus M, Petkova AT, Herzfeld J & Griffin RG Cross polarization in the tilted frame: assignment and spectral simplification in heteronuclear spin systems. *Molecular Physics* 95, 1197–1207 (1998).
24. Traaseth NJ et al. Structural and dynamic basis of phospholamban and sarcolipin inhibition of $\text{Ca}(2+)\text{-ATPase}$. *Biochemistry* 47, 3–13 (2008). [PubMed: 18081313]
25. Sa-Pessoa J et al. SATP (YaaH), a succinate-acetate transporter protein in *Escherichia coli*. *Biochem J* 454, 585–95 (2013). [PubMed: 23844911]
26. Sun P et al. Crystal structure of the bacterial acetate transporter SatP reveals that it forms a hexameric channel. *J Biol Chem* (2018).
27. Qiu B et al. Succinate-acetate permease from *Citrobacter koseri* is an anion channel that unidirectionally translocates acetate. *Cell Res* 28, 644–654 (2018). [PubMed: 29588525]
28. Igumenova TI et al. Assignments of carbon NMR resonances for microcrystalline ubiquitin. *J Am Chem Soc* 126, 6720–7 (2004). [PubMed: 15161300]
29. Buck B et al. Overexpression, purification, and characterization of recombinant Ca-ATPase regulators for high-resolution solution and solid-state NMR studies. *Protein Expression and Purification* 30, 253–261 (2003). [PubMed: 12880775]
30. Hing AW & Schaefer J Two-dimensional rotational-echo double resonance of $\text{Val1-}[1-^{13}\text{C}]\text{Gly2-}[^{15}\text{N}]\text{Ala3-gramicidin A}$ in multilamellar dimyristoylphosphatidylcholine dispersions. *Biochemistry* 32, 7593–604 (1993). [PubMed: 7687877]
31. Gullion T & Schaefer J Development of REDOR rotational-echo double-resonance NMR. *Journal of Magnetic Resonance* 81, 196 (1989).
32. Gullion T, Baker DB & Conradi MS New, compensated Carr-Purcell sequences. *Journal of Magnetic Resonance* 89, 479–484 (1990).
33. Fung BM, Khitritin AK & Ermolaev K An improved broadband decoupling sequence for liquid crystals and solids. *J Magn Reson* 142, 97–101 (2000). [PubMed: 10617439]
34. Franks WT, Kloeppe KD, Wylie BJ & Rienstra CM Four-dimensional heteronuclear correlation experiments for chemical shift assignment of solid proteins. *J Biomol NMR* 39, 107–31 (2007). [PubMed: 17687624]
35. Takegoshi K N., S; and Terao T $^{13}\text{C-}^1\text{H}$ dipolar-assisted rotational resonance in magic-angle spinning NMR. *Chemical Physics Letters* 344, 631–637 (2001).

36. Mote KR, Gopinath T & Veglia G Determination of structural topology of a membrane protein in lipid bilayers using polarization optimized experiments (POE) for static and MAS solid state NMR spectroscopy. *J Biomol NMR* 57, 91–102 (2013). [PubMed: 23963722]
37. Banigan JR & Traaseth NJ Utilizing afterglow magnetization from cross-polarization magic-angle-spinning solid-state NMR spectroscopy to obtain simultaneous heteronuclear multidimensional spectra. *J Phys Chem B* 116, 7138–44 (2012). [PubMed: 22582831]
38. Zhang Y et al. Resonance assignment and three-dimensional structure determination of a human alpha-defensin, HNP-1, by solid-state NMR. *J Mol Biol* 397, 408–22 (2010). [PubMed: 20097206]
39. Ekanayake EV, Fu R & Cross TA Structural Influences: Cholesterol, Drug, and Proton Binding to Full-Length Influenza A M2 Protein. *Biophys J* 110, 1391–9 (2016). [PubMed: 27028648]
40. Pines A, Waugh JS & Gibby MG Proton-Enhanced Nuclear Induction Spectroscopy - Method for High-Resolution Nmr of Dilute Spins in Solids. *Journal of Chemical Physics* 56, 1776 (1972).
41. Tang W & Nevzorov AA Repetitive cross-polarization contacts via equilibration-re-equilibration of the proton bath: Sensitivity enhancement for NMR of membrane proteins reconstituted in magnetically aligned bicelles. *J Magn Reson* 212, 245–8 (2011). [PubMed: 21784682]
42. Gopinath T, Mote KR & Veglia G Proton evolved local field solid-state nuclear magnetic resonance using Hadamard encoding: theory and application to membrane proteins. *J Chem Phys* 135, 074503 (2011). [PubMed: 21861572]
43. Gopinath T & Veglia G Sensitivity enhancement in static solid-state NMR experiments via single- and multiple-quantum dipolar coherences. *J Am Chem Soc* 131, 5754–6 (2009). [PubMed: 19351170]
44. Gopinath T & Veglia G Multiple acquisition of magic angle spinning solid-state NMR experiments using one receiver: application to microcrystalline and membrane protein preparations. *J Magn Reson* 253, 143–53 (2015). [PubMed: 25797011]
45. Hartmann SR & Hahn EL Nuclear Double Resonance in the Rotating Frame. *Physical Review* 128, 2042–2053 (1962).
46. Jain S, Bjerring M & Nielsen NC Efficient and Robust Heteronuclear Cross-Polarization for High-Speed-Spinning Biological Solid-State NMR Spectroscopy. *J Phys Chem Lett* 3, 703–8 (2012). [PubMed: 26286276]
47. Daviso E, Eddy MT, Andreas LB, Griffin RG & Herzfeld J Efficient resonance assignment of proteins in MAS NMR by simultaneous intra- and inter-residue 3D correlation spectroscopy. *J Biomol NMR* 55, 257–65 (2013). [PubMed: 23334347]
48. Tosner Z et al. Overcoming Volume Selectivity of Dipolar Recoupling in Biological Solid-State NMR Spectroscopy. *Angew Chem Int Ed Engl* 57, 14514–14518 (2018). [PubMed: 29989288]
49. Manu VS & Veglia G Optimization of identity operation in NMR spectroscopy via genetic algorithm: Application to the TEDOR experiment. *J Magn Reson* 273, 40–46 (2016). [PubMed: 27744147]
50. Paulson EK, Martin RW & Zilm KW Cross polarization, radio frequency field homogeneity, and circuit balancing in high field solid state NMR probes. *J Magn Reson* 171, 314–23 (2004). [PubMed: 15546758]
51. Tosner Z et al. Radiofrequency fields in MAS solid state NMR probes. *J Magn Reson* 284, 20–32 (2017). [PubMed: 28946058]
52. Tekely P & Goldman M Radial-field sidebands in MAS. *J Magn Reson* 148, 135–41 (2001). [PubMed: 11133286]
53. Zhang R, Mroue KH & Ramamoorthy A Proton-Based Ultrafast Magic Angle Spinning Solid-State NMR Spectroscopy. *Acc Chem Res* 50, 1105–1113 (2017). [PubMed: 28353338]
54. Andreas LB, Le Marchand T, Jaudzems K & Pintacuda G High-resolution proton-detected NMR of proteins at very fast MAS. *Journal of Magnetic Resonance* 253, 36–49 (2015). [PubMed: 25797003]
55. Demers JP, Chevelkov V & Lange A Progress in correlation spectroscopy at ultra-fast magic-angle spinning: Basic building blocks and complex experiments for the study of protein structure and dynamics. *Solid State Nuclear Magnetic Resonance* 40, 101–113 (2011). [PubMed: 21880471]

56. Zhou DH et al. Proton-Detected Solid-State NMR Spectroscopy of Fully Protonated Proteins at 40 kHz Magic-Angle Spinning. *Journal of the American Chemical Society* 129, 11791–11801 (2007). [PubMed: 17725352]
57. Struppe J et al. Expanding the horizons for structural analysis of fully protonated protein assemblies by NMR spectroscopy at MAS frequencies above 100 kHz. *Solid State Nuclear Magnetic Resonance* 87, 117–125 (2017). [PubMed: 28732673]
58. Wang S et al. Nano-mole scale sequential signal assignment by (1)H-detected protein solid-state NMR. *Chem Commun (Camb)* 51, 15055–8 (2015). [PubMed: 26317132]
59. Reif B Ultra-high resolution in MAS solid-state NMR of perdeuterated proteins: implications for structure and dynamics. *J Magn Reson* 216, 1–12 (2012). [PubMed: 22280934]
60. Wickramasinghe NP et al. Nanomole-scale protein solid-state NMR by breaking intrinsic 1HT1 boundaries. *Nature methods* 6, 215–218 (2009). [PubMed: 19198596]
61. Barnes AB et al. High-Field Dynamic Nuclear Polarization for Solid and Solution Biological NMR. *Appl Magn Reson* 34, 237–263 (2008). [PubMed: 19194532]

**Figure 1:**

A. Pulse sequences for the conventional 2D Z-filtered TEDOR experiment. **B.** Hybrid pulse sequence (TEDOR-NCX) that combines TEDOR and NCA (or NCO) experiments. **C.** 1D spectrum of U- ^{13}C , ^{15}N SLN recorded using conventional TEDOR experiment (black). **D.** 1D TEDOR and NCA spectra of U- ^{13}C , ^{15}N SLN acquired simultaneously with the TEDOR-NCX pulse sequence (blue and red). The phase cycles were $\phi_1=y, -y, y, -y$. $\phi_2=y, y, -y, -y$, and $\phi_{\text{receiver}}=y, -y, -y, y$. XY-4 phase cycling scheme was applied for ^{15}N π pulses during TEDOR mixing periods. States mode detection of t_1 dimension was obtained by switching the ϕ^* phase between y and $-x$.

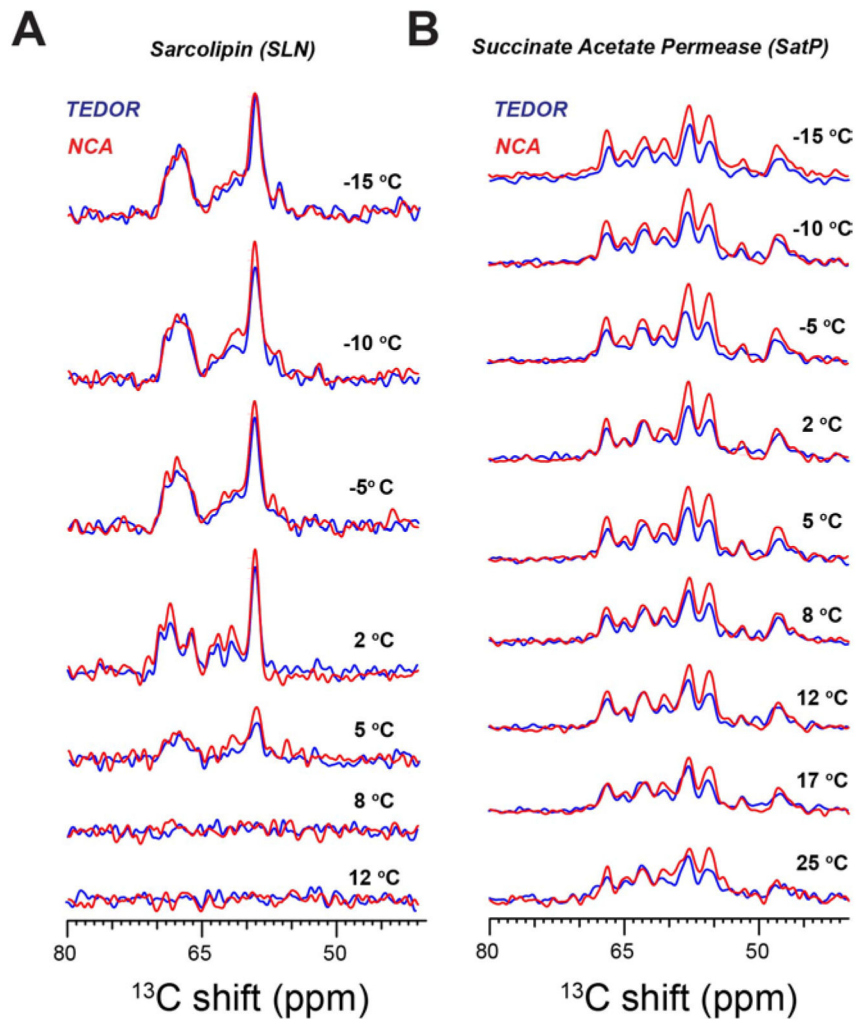


Figure 2: Temperature dependence of the $^{13}\text{C}\alpha$ signal intensities of 1D TEDOR and NCA spectra of **A.** single transmembrane protein U- ^{13}C , ^{15}N SLN, and **B.** six transmembrane U- ^{13}C , ^{15}N SatP. All spectra were acquired using TEDOR-NCA pulse sequence reported in Figure 1B.

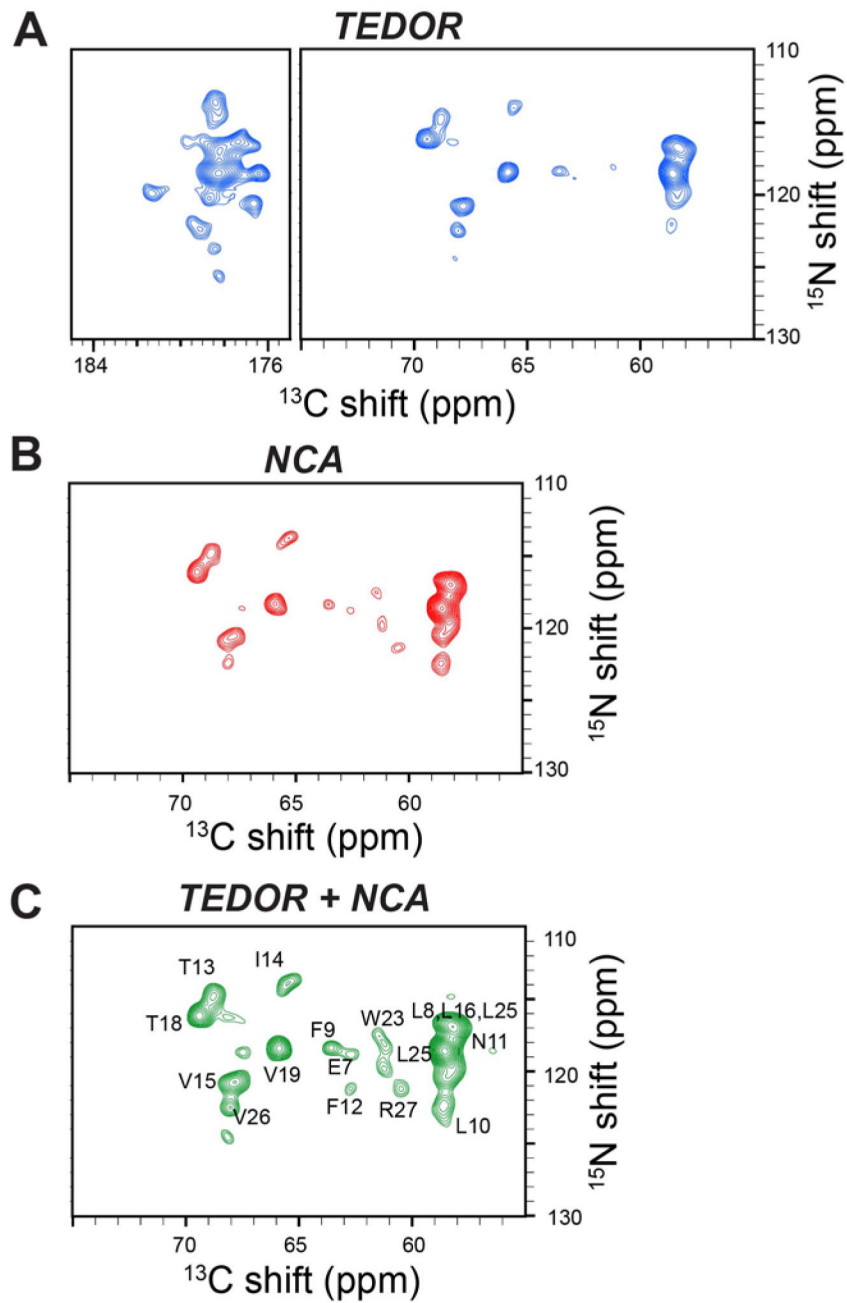


Figure 3:
A. 2D TEDOR spectrum of SLN (blue); **B.** 2D NCA spectrum of SLN (red). Both A and B were acquired simultaneously using the TEDOR-NCA pulse sequence. **C.** Sum of the TEDOR and NCA spectra. The resonances in the spectrum have an average sensitivity enhancement of 32% for $^{13}\text{C}\alpha$ region. All the spectra were plotted at same noise level.

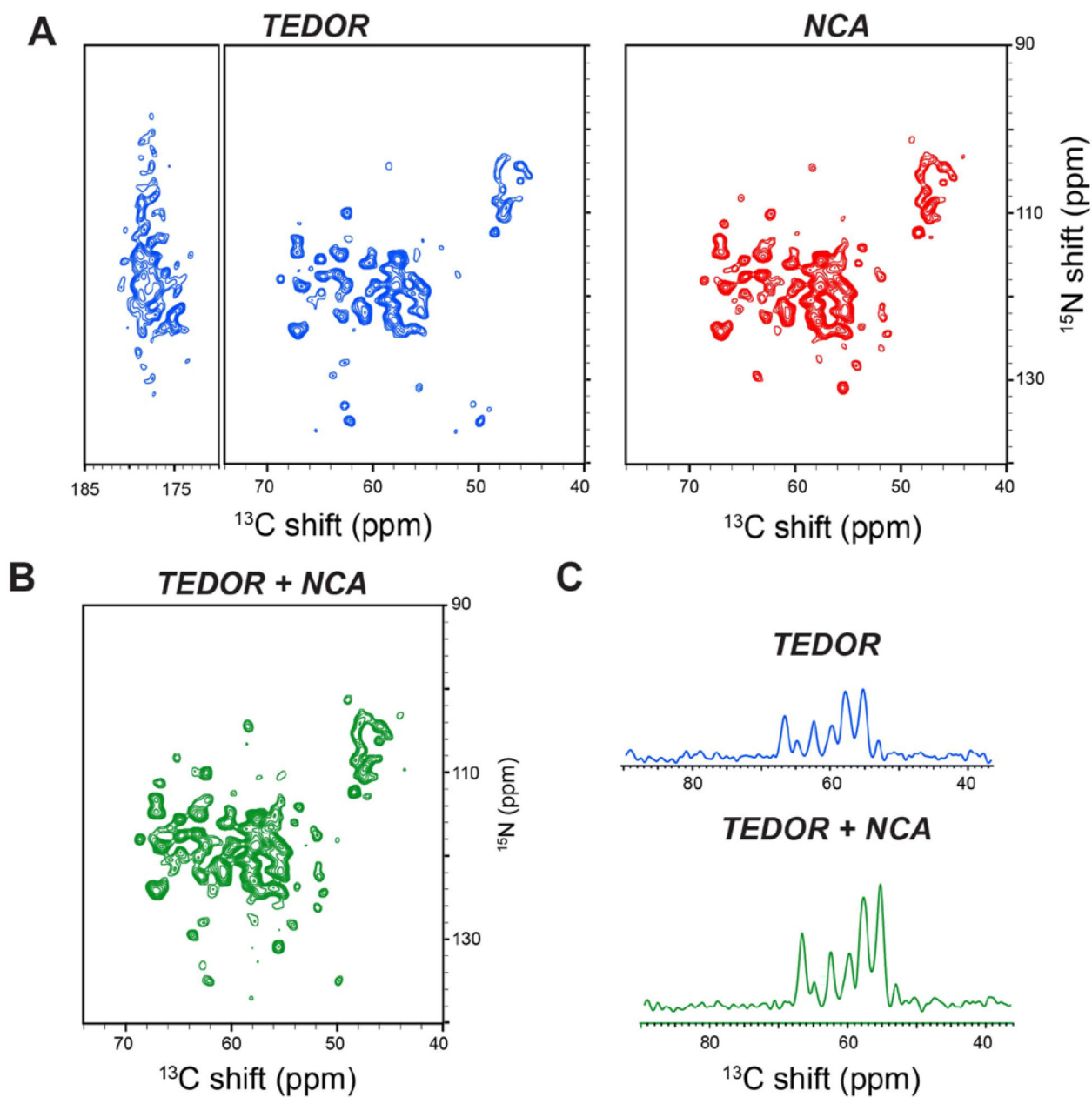
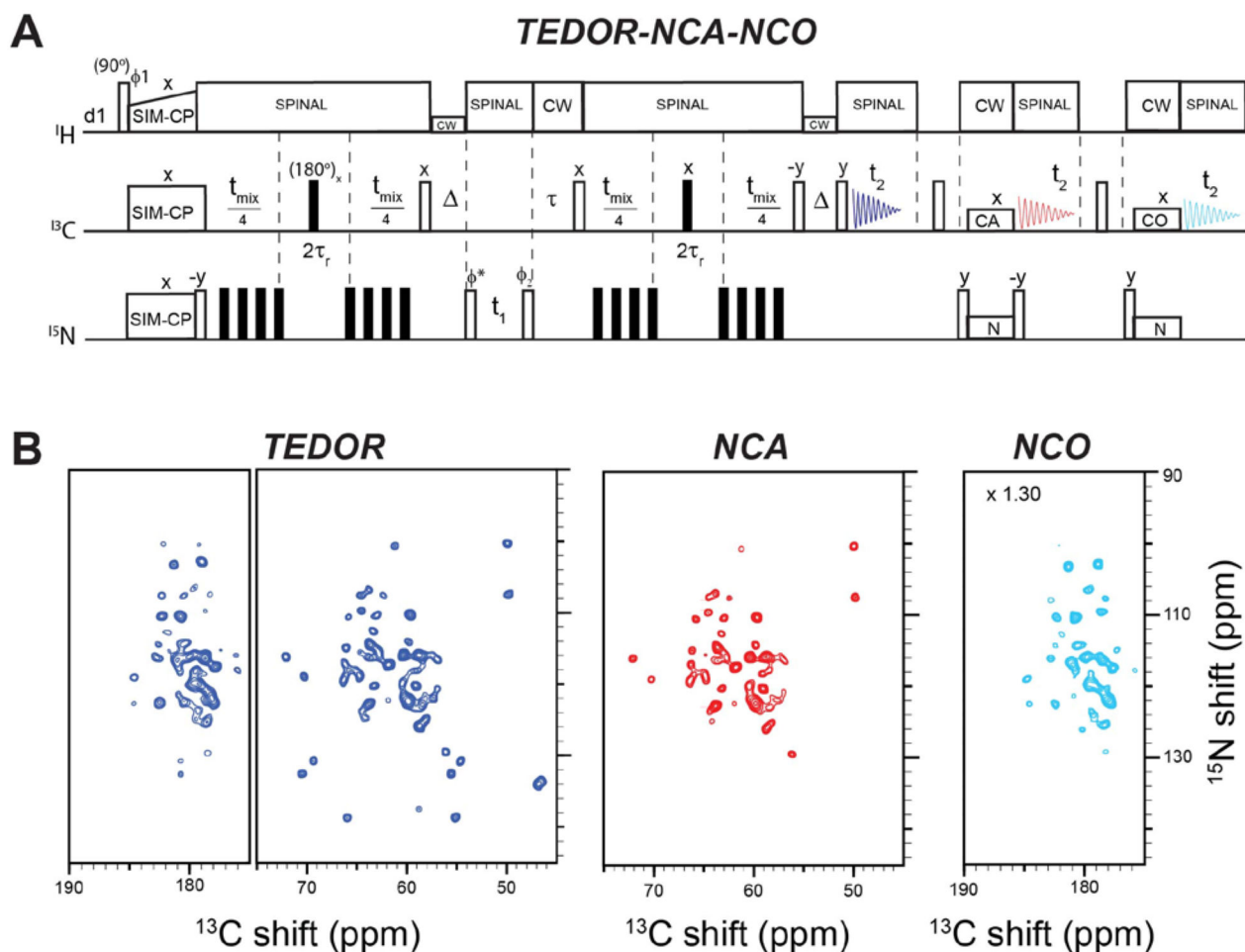
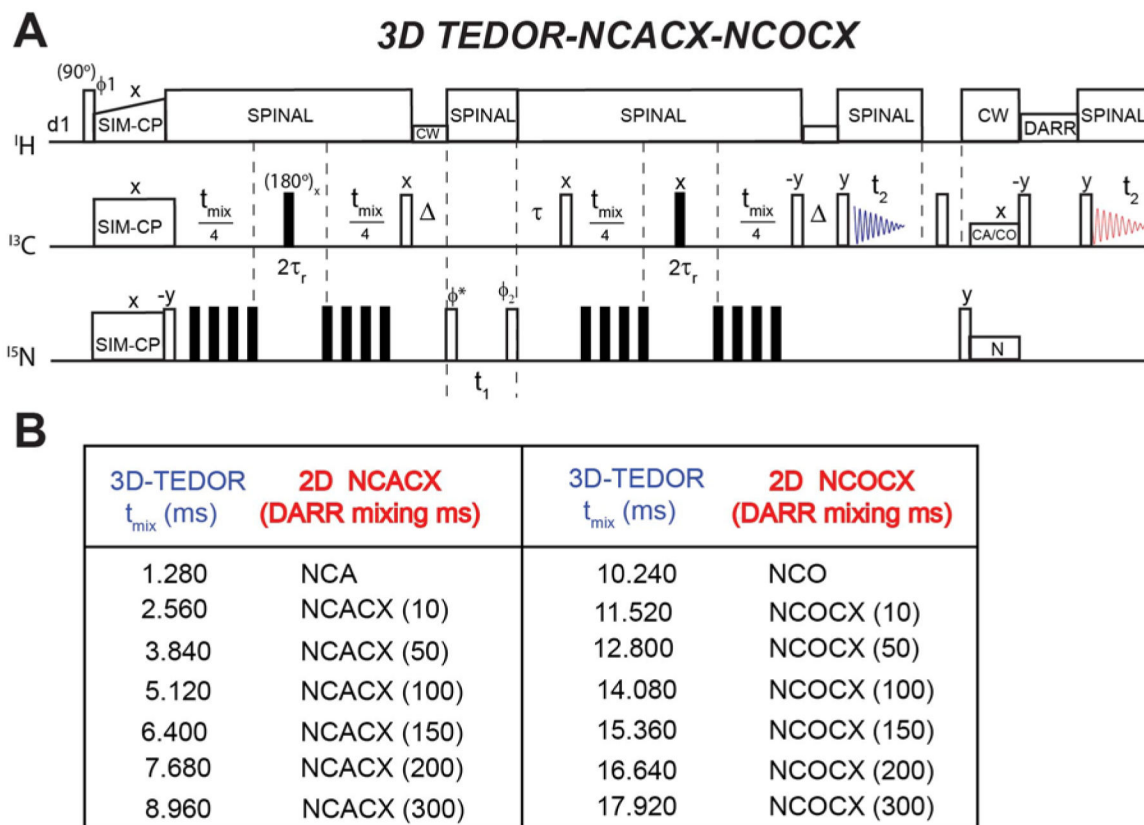


Figure 4:

A. 2D TEDOR and NCA spectra of SatP acquired simultaneously using the TEDOR-NCA pulse sequence. B. Sum of the 2D TEDOR and NCA spectra showing an average sensitivity enhancement of 60% for $^{13}\text{C}\alpha$ region with respect to the conventional TEDOR experiment. All the 2D spectra were plotted at same noise level. C. 1D cross sections of TEDOR and TEDOR+NCA spectra along ^{15}N dimension at 119 ppm, showing the signal enhancement.

**Figure 5:**

A. TEDOR-NCA-NCO pulse sequence for simultaneous acquisition of TEDOR, NCA and NCO experiments. **B.** Spectra of U- ^{13}C - ^{15}N ubiquitin microcrystalline sample recorded with the pulse sequence in A. The 2D spectra of TEDOR and NCA were drawn at same noise level, whereas NCO spectrum was multiplied by 1.30 to show all the resonances.

**Figure 6:**

A. Hybrid pulse sequence for simultaneous acquisition of 3D TEDOR, NCACX, and NCOCX experiments. **B.** Table reporting the different mixing times for TEDOR and DARR used for the experiments on the NAVL peptide (see also Figure 7).

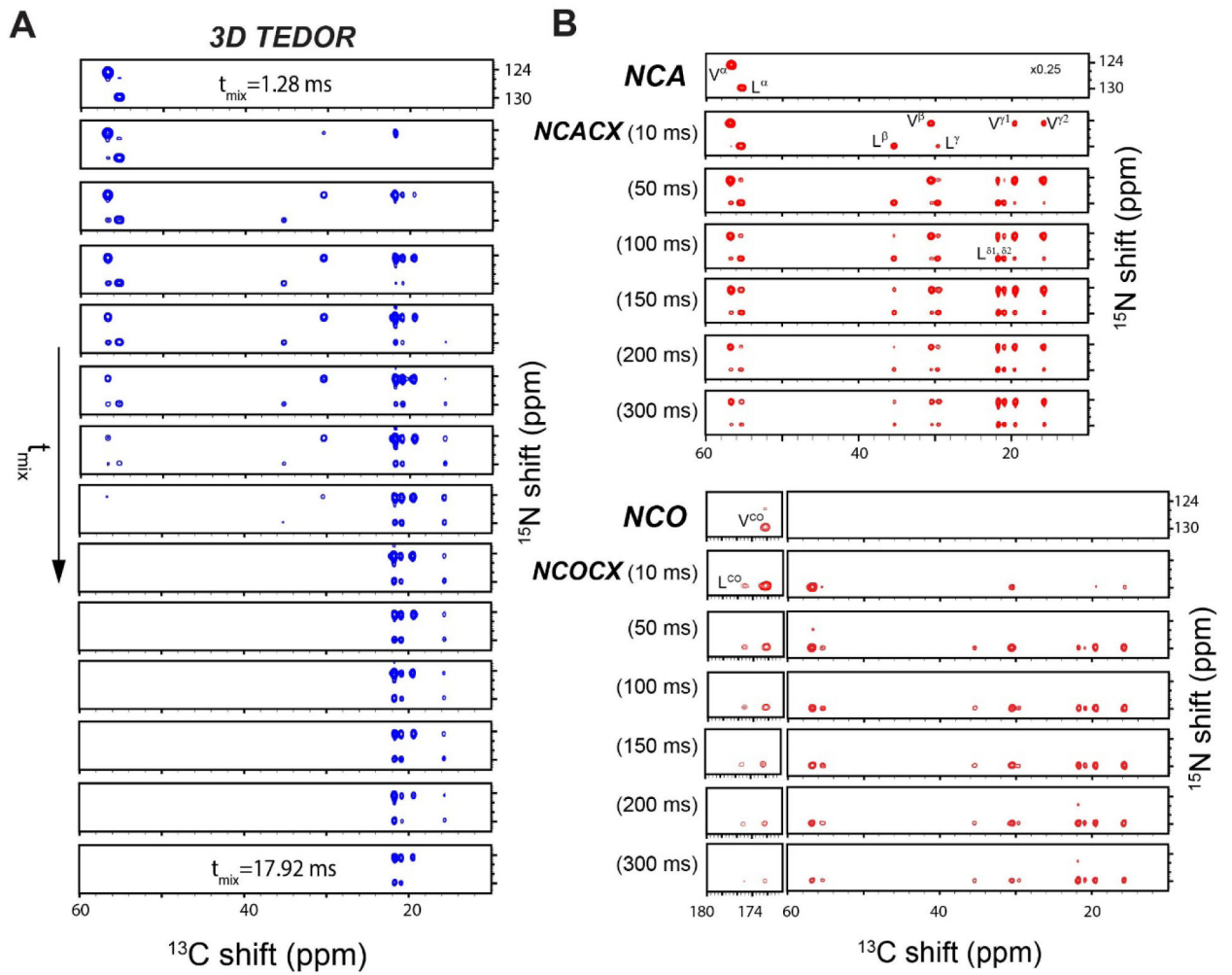


Figure 7:
 3D spectra of NAVL dipeptide acquired simultaneously with the TEDOR-NCACX-NCOCX pulse sequence. **A.** TEDOR spectra at different mixing times. **B.** NCACX, and NCOCX spectra at different DARR mixing times.

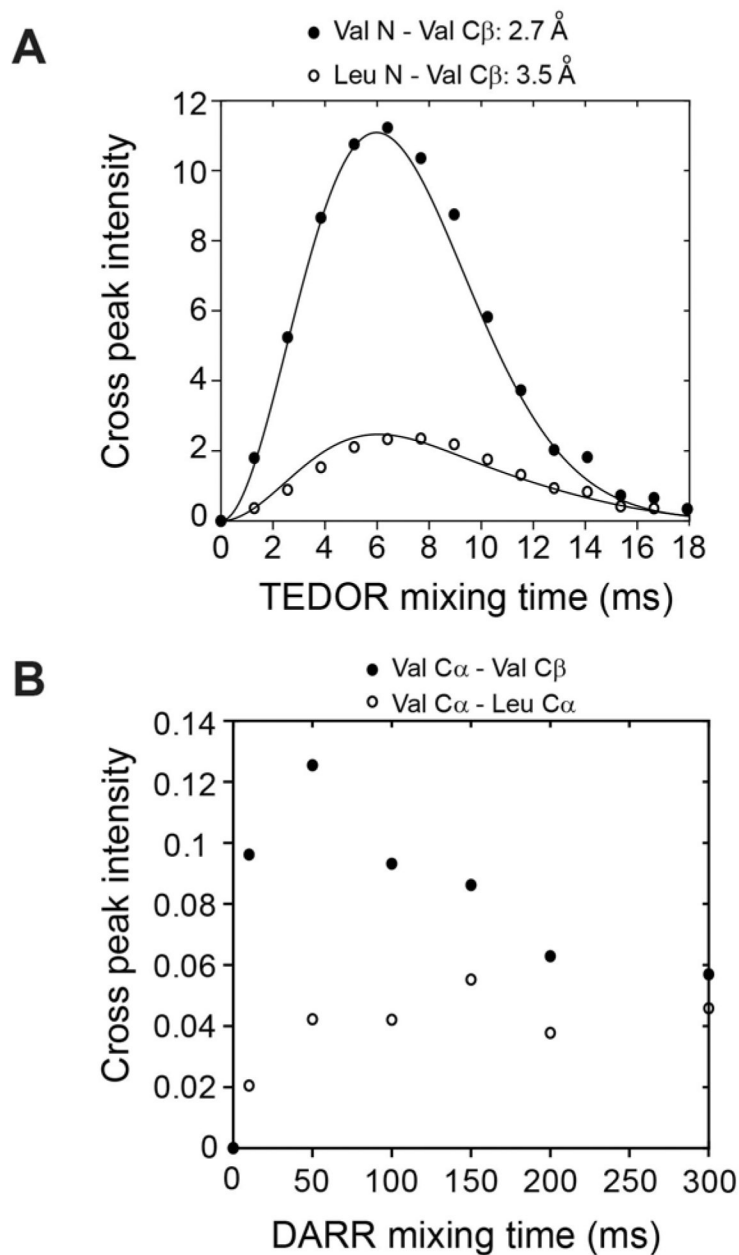


Figure 8: Simultaneous measurement of ^{15}N - ^{13}C and ^{13}C - ^{13}C distance restraints on NAVL dipeptide from 3D-TEDOR-NCACX-NCOCX spectra of Figure 7. **A.** 3D TEDOR cross peak intensities as a function of the mixing time. The Val N to Val C β cross peaks are indicated as filled circles. The cross peaks for Leu N to Val C β are indicated with open circles. The cross peak intensities were fit with simulated curves using 2.7 and 3.5 Å, respectively. **B.** NCACX cross peak intensities between Val C α -C β and Val C α -Leu C α plotted at different DARR mixing times.

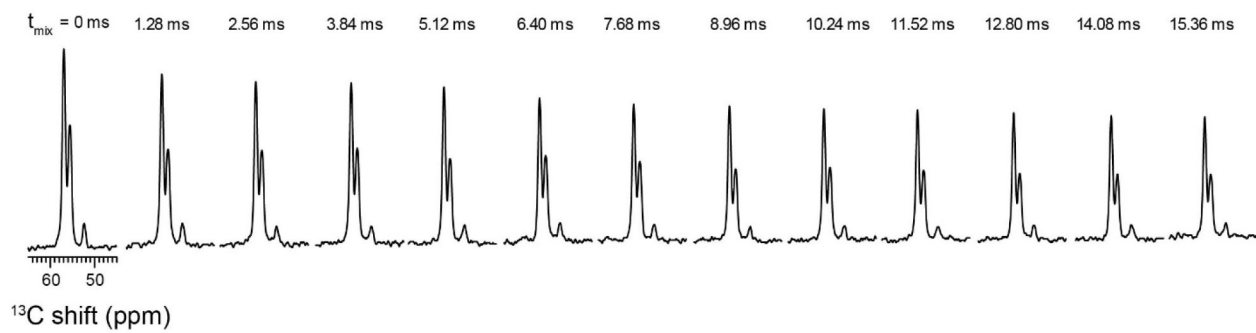


Figure 9: Effects of the TEDOR 180° pulses on the ^{15}N z-magnetization of the NAVL dipeptide as monitored by 1D NCA spectra. The spectra refer to the second acquisition of the pulse sequence reported in Figure 6A.